AD-A110 027 NAVAL SURFACE WEAPONS CENTER SILVER SPRING MD F/G 9/1
SLOW WAVE GYROTRON AMPLIFIER WITH A DIELECTRIC CENTER ROD.(U)
SEP 81 J Y CHOE, H S UHM
UNCLASSIFIED NSWC/TR-81-387 NL

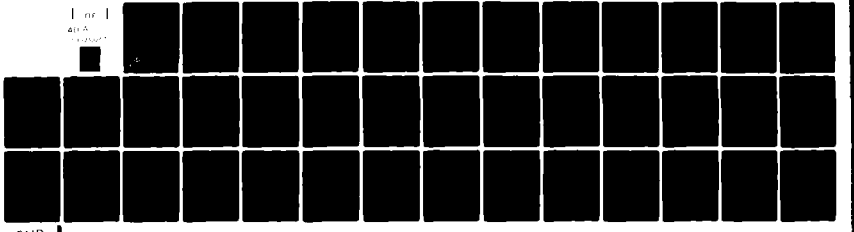

END
DATE FILMED
10-82
DTIC

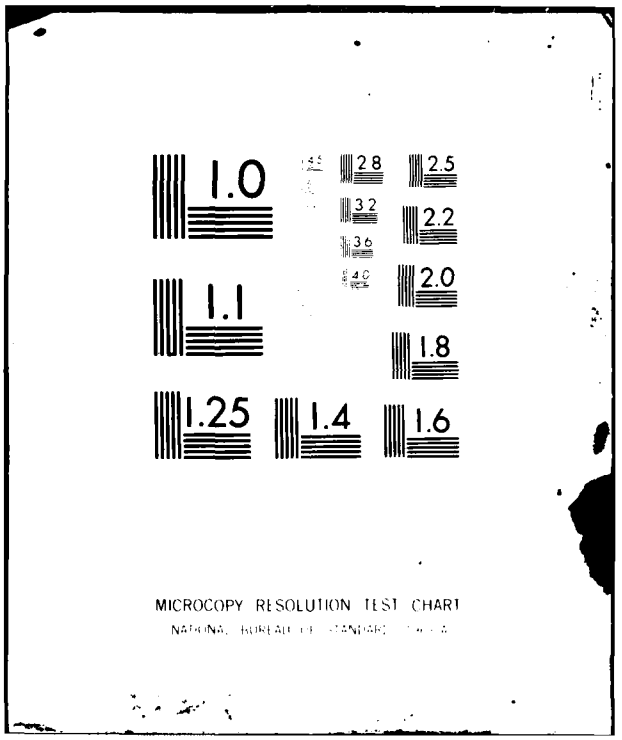
1.0
2.8
2.5
3.2
2.2
3.6
4.0
2.0
1.1
1.8
1.25
1.4
1.6
MICROCOPY RESOLUTION TEST CHART

LEVEL II

12

NSWC TR 81-387

AD A110027

SLOW WAVE GYROTRON AMPLIFIER WITH A DIELECTRIC CENTER ROD

BY JOON Y. CHOE HANS S. UHM

RESEARCH AND TECHNOLOGY DEPT.

SEPTEMBER 1981

NAVAL SURFACE WEAPONS CENTER

Dahlgren, Virginia 22448 • Silver Spring, Maryland 20910

UNCLASSIFIED

SECURITY CLASSIFICATION OF THIS PAGE *(When Data Entered)*

REPORT DOCUMENTATION PAGE	READ INSTRUCTIONS BEFORE COMPLETING FORM
1. REPORT NUMBER: NSWC/TR 81-387	2. GOVT ACCESSION NO.: AD-A110027
3. RECIPIENT'S CATALOG NUMBER:	
4. TITLE *(and Subtitle)*: Slow Wave Gyrotron Amplifier With a Dielectric Center Rod	5. TYPE OF REPORT & PERIOD COVERED: Final
	6. PERFORMING ORG. REPORT NUMBER:
7. AUTHOR(s): Joon Y. Choe and Han S. Uhm	8. CONTRACT OR GRANT NUMBER(s):
9. PERFORMING ORGANIZATION NAME AND ADDRESS: Naval Surface Weapons Center, Code R41, White Oak, Silver Spring, Maryland 20910	10. PROGRAM ELEMENT, PROJECT, TASK AREA & WORK UNIT NUMBERS: 61152N, ZR00001, ZR01109, 0
11. CONTROLLING OFFICE NAME AND ADDRESS:	12. REPORT DATE: September 1981
	13. NUMBER OF PAGES: 41
14. MONITORING AGENCY NAME & ADDRESS *(if different from Controlling Office)*:	15. SECURITY CLASS. *(of this report)*: UNCLASSIFIED
	15a. DECLASSIFICATION/DOWNGRADING SCHEDULE:
16. DISTRIBUTION STATEMENT *(of this Report)*: Approved for public release, distribution unlimited	
17. DISTRIBUTION STATEMENT *(of the abstract entered in Block 20, if different from Report)*:	
18. SUPPLEMENTARY NOTES:	
19. KEY WORDS *(Continue on reverse side if necessary and identify by block number)*: Gyrotron Amplifier; Microwave Amplifier; Slow Wave Gyrotron; Dielectric Material	

20. ABSTRACT *(Continue on reverse side if necessary and identify by block number)*:

The broad band capability of the gyrotron amplifier with a dielectric center rod is investigated. The dispersion relation for the TE mode perturbation is obtained, and the system parameters for the optimum bandwidth are obtained for a small axial velocity spread. It is found that the dielectric center rod extends the frequency range of the intermediate wavelength mode (IWM), and reduces the contribution of the troublesome short wavelength mode (SWM). The bandwidth and the gain due to the IWM for the center rod geometry are superior to those for the wall clad dielectric gyrotron.

DD FORM 1 JAN 73 1473 EDITION OF 1 NOV 65 IS OBSOLETE
S/N 0102-014-6601

UNCLASSIFIED

SECURITY CLASSIFICATION OF THIS PAGE *(When Data Entered)*

FOREWORD

The broad band capability of the gyrotron amplifier with a dielectric center rod is investigated. The dispersion relation for the TE mode perturbation is obtained, and the system parameters for the optimum bandwidth are obtained for a small axial velocity spread. It is found that the dielectric center rod extends the frequency range of the intermediate wavelength mode (IWM), and reduces the contribution of the troublesome short wavelength mode (SWM). The bandwidth and the gain due to the IWM for the center rod geometry are superior to those for the wall clad dielectric gyrotron.

Ira M Blatstein

IRA M. BLATSTEIN
By direction

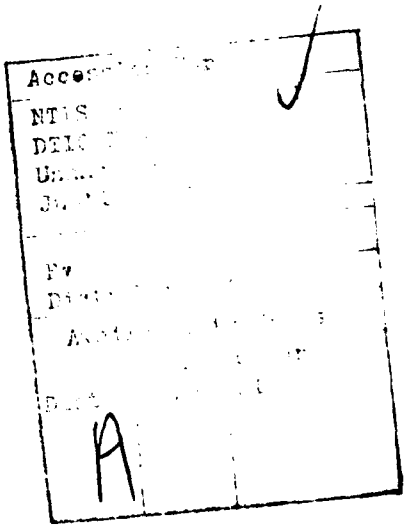

CONTENTS

ILLUSTRATIONS

ILLUSTRATIONS (Cont.)

TABLES

INTRODUCTION

Recently there have been numerous studies [1]-[6] on the dielectric loaded gyrotron for a wide band application. It has been found [2], [4], [6] that there exist three unstable modes characterized by their axial phase velocities (v_{ph}); the long wavelength mode (LWM, $v_{ph} > c$), the intermediate wavelength mode (IWM, $c > v_{ph} > c\varepsilon^{-1/2}$), and the short wavelength mode (SWM, $v_{ph} < c$). Here ε and c are the dielectric constant and the velocity of light. For a small axial velocity spread ($\lesssim 1\%$), two slow wave modes (IWM and SWM) yield very promising bandwidth capability [2], especially when two modes are mixed by placing the beam close to the axis [4], [6]. However, the nature of the SWM [2], [4], whose perturbed fields are almost entirely supported by the electron beam, not by the waveguide, raises the difficulties related to the excitation and collection of the electromagnetic waves [2], [4]. One possible solution to this difficulty is to utilize the dielectric material as a center rod [7], rather than as an outside wall loading [1]-[5]. By using dielectric material as a center rod, it will be shown that the frequency range of the IWM is extended, while the contribution of the troublesome SWM is minimized.

The dispersion relation for the gyrotron with a dielectric center rod has been derived by authors [7] for general azimuthal (θ) harmonic numbers (i.e. $\ell \neq 0$). In this paper, we will perform a detailed numerical investigation of this dispersion equation for a broad range of the physical parameters, and compare the results with those of the gyrotron with the outer dielectric loading [2], [4], [6]. For simplicity, the present investigation is limited to the azimuthally symmetric (i.e. $\ell = 0$), transverse electric (TE) perturbations. Moreover, in view of the relative insensitivity of the fast wave mode (LWM) to the system parameters [2], [6], [7], we will devote our attention only to

the slow wave modes (IWM and SWM). A complete parametric optimization process for wide bandwidth will be carried out, assuming that the axial velocity spread of the beam electrons is small (= 1%). The optimization is carried out in the spirit of maximizing the contribution of the IWM to the bandwidth, and minimizing that of the SWM. In addition, the perturbed field profiles are examined in order to distinguish the IWM and SWM.

The slow wave modes (IWM and SWM) for the center rod gyrotron do not compete each other in their contribution to the instability as much as for the wall clad configuration. This cooperative nature of the IWM and the SWM results in an extended IWM region compared to the wall clad geometry. That is, the SWM begins to contribute significantly at higher frequency than it does in the outside loaded gyrotron. On the other hand, it will be shown that the bandwidth itself for the center rod configuration is approximately as wide as that for the wall clad one (see Sec. III). Thus by putting the dielectric rod at the center, we are able to maintain about the same wide band capability, while eliminating some of the difficulties associated with the SWM.

A brief review for the derivation procedure of the dispersion relation will be given in Sec. II. The expressions for the perturbed fields are also given in Sec. II for later use. The optimization for the wide bandwidth with 1% of the axial velocity spread is carried out in Sec. III. The physical parameters to be optimized are the thickness ratio of the dielectric center rod (R_d/R_c), the dielectric constant (ε), the conducting wall radius (R_c), and the beam center location (R_0). In Sec. IV, the perturbed field profiles are investigated in order to examine the individual contribution of the IWM and the SWM to the bandwidth. Especially we compare these field profiles with those of the wall clad configuration. The summary of the comparison is given in the conclusion Section IV.

DISPERSION RELATION

The cross section of the gyrotron with a dielectric center rod is shown in Fig. 1. A cylindrical dielectric (ϵ) rod of radius R_d is located concentrically with the conducting wall of radius R_c. The hollow electron beam passes through the space between the dielectric center rod and the conducting wall. The individual electrons undergo the cyclotron motion with Lamor radii r_L about the beam center location R_0, under the influence of the constant applied axial magnetic field B_0. In addition, the electron beam moves downstream with the axial velocity. The cylindrical coordinates (r, θ, z) are employed.

The dispersion relation is derived within the framework of the Vlasov-Maxwell equations for the fields $\underline{E}(\underline{x},t)$ and $\underline{B}(\underline{x},t)$, and for the beam electron distribution function $f(\underline{x},\underline{p},t)$. Here $\underline{x}$, $\underline{p}$, and t refer to the spatial, momentum, and the time coordinates. Further, any quantity ψ is linearized according to

$$\psi(\underline{x},t) = \psi_0(r) + \psi_1(r)\ exp[i(kz - \omega t)] \tag{1}$$

with the equilibrium quantity ψ_0 and the small Fourier decomposed perturbation ψ_1. Note that we limit our attention to the azimuthally symmetric perturbation $(\partial/\partial\theta=0)$ with the frequency ω and the axial wavenumber k. Moreover, we will consider the transverse electric (TE, $E_{z1} = 0$) perturbation only. It is assumed that the beam is tenuous, and the beam thickness is small [1], [2], [4], [6], [7]. In order to examine the effect of the axial velocity spread, the equilibrium distribution function f_0 is assumed to be Lorentzian [2], [4], [6], [7] in the axial momentum p_z, that is,

$$f_0 \propto \hat{p}_z\ \Delta[(p_z - \hat{p}_z)^2 + \hat{p}_z^2\ \Delta^2]^{-1}. \tag{2}$$

Here $\hat{p}_z$ is the average axial linear momentum and Δ is the axial momentum spread ratio. The beam is further assumed to be monoenergetic with γmc^2, and the average transverse (axial) velocity is given by $c\beta_\perp$ ($c\beta_z$).

Since the details of the procedures in obtaining the dispersion relation are given in Ref. 7, here we present only the outline. Making use of the thin beam approximation and the boundary conditions on the azimuthal electric field $E_{\theta 1}$ at r=0, R_d, R_0, and R_c, within a normalizing factor we obtain the perturbed fields $\underline{E}_1$ and $\underline{B}_1$.

$$E_{\theta 1} = \begin{cases} J_1(y), & 0 \le r \le R_d \\ -\frac{\pi}{2}\,[A_{JN}\,J_1(x) - A_{JJ}\,N_1(x)], & R_d \le r \le R_0 \\ -\frac{\pi}{2}\,\frac{B_2}{B_3}\,[N_1(x_c)\,J_1(x) - J_1(x_c)\,N_1(x)], & R_0 \le r \le R_c \end{cases} \tag{3}$$

$$B_{r1} = -\frac{ck}{\omega}\,E_{\theta 1}, \quad B_{z1} = -\frac{ic}{\omega}\,\frac{1}{r}\,\frac{\partial}{\partial r}\,(rE_{\theta 1}). \tag{4}$$

The jump condition on B_{z1} across the beam furnishes the desired dispersion relation. Namely,

$$\frac{B_N}{B_D} = -\frac{\nu\beta_\perp^2\,c^2}{2\gamma\,R_0^2\,[\omega-\omega_B + i|k|\,c\beta_z\,\gamma\Delta/\gamma_z^3]^2}, \tag{5}$$

with the wave admittance [1], [2], [4], [6], [7] B_N/B_D is given by

$$B_N = 2B_1,\ B_D = -\pi x_0^2\, B_2\, B_3,$$

$$B_1 = J_1(x_c)\, A_{JN} - N_1(x_c)\, A_{JJ},$$

$$B_2 = J_1(x_0)\, A_{JN} - N_1(x_0)\, A_{JJ}, \tag{6}$$

$$B_3 = J_1(x_0)\, N_1(x_c) - N_1(x_0)\, J_1(x_c),$$

$$\begin{Bmatrix} A_{JJ} \\ A_{JN} \end{Bmatrix} \equiv y_d\, J_0(y_d) \begin{Bmatrix} J_1(x_d) \\ N_1(x_d) \end{Bmatrix} - x_d \begin{Bmatrix} J_0(x_d) \\ N_0(x_d) \end{Bmatrix} J_1(y_d)$$

The arguments of the first (J) and the second (N) kind Bessel functions are

$$\begin{Bmatrix} y^2 \\ y_d^2 \end{Bmatrix} \equiv \left(\frac{\omega^2}{c^2}\,\varepsilon - k^2\right) \begin{Bmatrix} r^2 \\ R_d^2 \end{Bmatrix}, \tag{7}$$

$$\begin{Bmatrix} x^2 \\ x_d^2 \\ x_0^2 \\ x_c^2 \end{Bmatrix} \equiv \left(\frac{\omega^2}{c^2} - k^2\right) \begin{Bmatrix} r^2 \\ R_d^2 \\ R_0^2 \\ R_c^2 \end{Bmatrix}$$

In Eq. (5), the Doppler-shifted beam mode ω_B is defined by

$$\omega_B \equiv kc\beta_z + \omega_c/\gamma, \tag{8}$$

the Budker parameter (ν) is given by $\nu \equiv Ne^2/mc^2$, $\omega_c \equiv eB_0/mc$ is the non-relativistic electron cyclotron frequency, and $\gamma_z \equiv (1 - \beta_z^2)^{-1/2}$ is the axial mass factor. Here N is the total number of electrons per unit axial length, and (-e) and m are the charge and the rest mass of the electron. It is easy to show that the dispersion relation in Ref. 7 yields the identical result (Eq. (5)) in the limit of ℓ=0.

The dispersion relation (5) is numerically solved for the axial wave-number k in terms of the frequency ω, when other beam and geometric parameters (ν, $\beta_\perp$, β_z, Δ, R_0, ε, R_c, R_d) are given. If the solution k is complex, the mode is unstable, and the gain is given by the negative value of the imarginary part of k (i.e. $-k_i \equiv -\text{Im}(k)$, when $k_i < 0$). The characteristics of the unstable modes thus obtained are very similar to those with the wall-clad dielectric gyrotron [2]. The TE perturbation exhibits three unstable modes; one fast wave mode (LWM) and two coexisting slow wave modes (IWM and SWM) separated by a stable band near ω=ck line. Both the LWM and IWM are originated from the unstable coupling of the beam mode ω_B (Eq. (8)) and the beam-free waveguide mode ω_G (the solution of $B_N = 0$ in Eqs. (5)-(6)). On the other hand, the SWM is driven by a quasi-static magnetic dipole moment instability [6], [8], characterized by highly localized perturbed fields near the beam location ([2], [4], [6] and see Sec. IV). As in the case of the wall clad geometry, the reduction in the gain due to the axial velocity spread (Δ in Eq. (2)) is the least for the LWM, moderate for the IWM, and the largest for the SWM. On the other hand, the bandwidth at small axial velocity spread ($\Delta \lesssim 1\%$) is the broadest for the SWM, intermediate for the IWM, and the narrowest for the LWM. Since our objective is to achieve the wide bandwidth, we will concentrate only the slow waves (IWM and SWM) in the remainder of this paper. In view of the difficulties associated with the

SWM (excitation and collection of the electromagnetic waves), we attempt to find the parameter conditions where the IWM shows a wide bandwidth, over which the SWM is substantially suppressed.

In light of our intention to minimize the SWM contribution, there are several ways to distinguish the integrated two slow waves (IWM and SWM). One method is to utilize the different vulnerability of their gains on the velocity spread (Δ). Although we choose Δ=1% for our investigation, we therefore examine the gain for Δ=3% as well. If the gain is substantial for both Δ=1% and 3%, we identify this instability due to the IWM. On the other hand, if the gain is greatly reduced for Δ=3%, we label them as the SWM. The other method to distinguish the two modes is to examine the perturbed field profile. If the field profile is very similar to that of the beam-free waveguide, then the instability is due to the beam-waveguide coupling IWM. If, however, the field profile is highly localized near the beam location, we attribute the gain to the SWM. The former method is used in Sec. III and the latter in Sec. IV.

PARAMETRIC OPTIMIZATION

In this section we will obtain the optimized physical parameters for the wide band gyrotron amplifier; the thickness ratio of the dielectric center rod (R_d/R_c), the conducting wall radius (R_c), the dielectric constant (ε), and the beam location (R_0). We again emphasize that the optimization is for the bandwidth due to the IWM, minimizing the contribution of the troublesome SWM. In the remainder of this paper, we assume the following beam parameters.

$$\beta_\perp = 0.4,\ \beta_z = 0.2,\ \nu = 0.002, \tag{9}$$

corresponding to the 60.3 KV of the anode voltage and 6.8 Amp. of the total axial current. For future reference, we also define

$$R_c^0 \equiv 4.197\ c/\omega_c. \tag{10}$$

It can be shown that R_c^0 is the optimized wall radius when the dielectric is absent [2], [4], [6]. The axial velocity spread (Δ) of the beam is assumed to be small (Δ=1%). However, in order to examine the contribution of the SWM (to be minimized), case for Δ=3% is also examined as for reference.

Since the IWM results from the coupling of the beam mode ω_B(Eq. (8)) and the beam-free waveguide mode ω_G (B_N=0 in Eq. (6)), much information on the IWM can be extracted by examining the two modes, $\omega_B(\beta_\perp, B_z, \omega_c)$ and $\omega_G(R_d, R_c, \varepsilon)$. In Fig. 2, a schematic diagram of the mode characteristics is given in the space of the conducting wall radius (R_c) and the dielectric constant (ε). The dispersion curves for the parameters denoted by A, B and C are schematically shown in the upper corner. When the beam mode ω_B (the straight line in the upper corner diagram) grazes the waveguide mode ω_G (case B), the IWM gain is maximum. For the parameters above the maximum gain curve (solid curve in Fig. 2),

ω_B intersects ω_G more than one time (case C), and for the parameters below the maximum gain line, ω_B does not intersect ω_G at all (case A). Since the IWM gain is maximum at the ω_B-ω_G intersecting points, it is obvious that the SWM is dominant when the parameters (R_c and ε) are well below the maximum IWM gain line, while at near and above it, the IWM is dominant as shown. Above the maximum IWM gain line, where ω_B intersects ω_G more than one time, the gain yields multiple maxima in ω-space with a valley in between. Therefore, we expect that the maximum bandwidth line (broken) is located slightly above the maximum gain line (solid). Along the maximum bandwidth line, the gain at the valley in k_i-ω diagram is just high enough so that the bandwidth covers the both maxima, to yield broadest bandwidth. As one moves further above the maximum bandwidth line, the valley of k_i-ω diagram is too deep to extend the bandwidth to both maxima, thereby abruptly decreasing the bandwidth. All these arguments will be later confirmed in the numerical investigations.

After seeing that the beam-waveguide grazing condition (case B in Fig. 2) plays an important role in predicting both the gain and the bandwidth of the IWM, we now proceed to find the grazing conditions for the beam parameters given in Eq. (9). The results are summarized in Fig. 3, where the values of the wall radius (R_c, solid lines) and the dielectric constant (ε, broken lines) that make the beam mode graze the waveguide mode (upper corner) are plotted. The thickness ratio of the dielectric rod (R_d/R_c) varies from 0.10 to 0.35 with 0.05 increment. The results in Fig. 3 are similar to those for the wall clad configuration (Fig. 7 in Ref. 2). However, there are several noteworthy differences. In general, the center rod configuration yields larger wall radius, and smaller dielectric constant compared to the wall clad gyrotron. For example, for the same thickness ratio (R_d/R_c = 0.20 for the

center rod, $R_w/R_c = 0.80$ for the wall clad, where R_w is the inner radius of the dielectric material), $R_c/R_c^0 = 0.7 - 0.8$, $\epsilon = 12 - 13$ in the IWM frequency range for the center rod, and $R_c/R_c^0 = 0.5 - 0.6$, $\epsilon = 13 - 15$ for the wall clad case. The larger wall radius for the center rod configuration may be an advantage when the operating frequency is very high. We note from Fig. 3 that for the thickness ratio $R_d/R_c = 0.20$, the grazing R_c or ϵ remains relatively unchanged over the IWM frequency range (i.e. $\omega/\omega_c > 1.1$). That is, at this dielectric configuration ($R_d/R_c = 0.20$), the beam mode grazes or nearly grazes the waveguide mode for a broad range of the frequency in the IWM region, thereby resulting in a wide bandwidth. We therefore conclude that the optimized rod thickness ratio is given by $R_d/R_c = 0.20$. However, we also note that the value of ϵ or R_c, although relatively flat, varies more sensitively than that for the wall clad case [2]. This enhanced sensitivity aids the center rod gyrotron in achieving wider bandwidth, although at smaller gain, compared to the wall clad case. This will be confirmed later in the numerical investigations.

The relative sensitivity of the gain to the variation of R_c or ϵ for the center rod configuration necessitates additional optimization investigations on R_c and ϵ. These are illustrated in Figs. 4 and 5. With the beam parameters (9) and the optimized rod thickness ratio $R_d/R_c = 0.20$, the linear gain ($-k_i$) is numerically obtained from the dispersion relation (5), as a function of the frequency (ω) for various values of the wall radius R_c and the dielectric constant ϵ. The maximum value of the gain ($-k_i^{max}$) in the k_i-ω diagram is shown in Fig. 4, which determines the maximum gain curve in the R_c - ϵ space in Fig. 2. Although the chosen velocity spread (Δ) is 1%, those for Δ=3% are also shown as a reference. For Δ=1%, the plot of k_i vs. ω yields multiple maxima for ϵ higher than a

certain value, denoted in the figure with dotted lines. This multiple maxima phenomenon is expected from the considerations in Fig. 2, corresponding to the case C. On the other hand, for Δ=3%, the k_i-ω curve yield only single peak. This can be explained from the greater reduction rate of the gain at higher frequencies for a large spread [2], [4], [6]. That is, the peak at higher frequency is quenched more rapidly when the spread is large. The actual bandwidth for the same parameter in Fig. 4 is shown in Fig. 5. The bandwidth is defined by the full width of the real frequency, at which the linear gain drops to $\exp(-\frac{1}{2})$ of its maximum value. Of course, the bandwidth is normalized by its mean frequency $\bar{\omega}$. This definition of the bandwidth is somewhat unconventional, but it serves the comparison purposes. For a small spread (Δ=1%), the bandwidth curve in Fig. 5 yields interesting results. For given wall radius (R_c), as the dielectric constant (ϵ) is increased, the bandwidth decreases, and then increases to give a local peak, followed by an abrupt decrease. Although the bandwidth can be much wider for ϵ lower than that giving local maximum, we attribute this wider bandwidth mainly to the SWM contribution. This is evident from the bandwidth curve for Δ=3%. At ϵ lower than that giving local maxima for Δ=1%, the bandwidth is actually narrower for Δ=3%. In view of the more sensitive nature of the SWM to the velocity spread compared to that of the IWM, we therefore conclude that the wider bandwidth for low ϵ at Δ=1% is due to the SWM. Since our optimization is for the IWM only (suppressing the SWM), the optimized bandwidth of the desired IWM at Δ=1% corresponds to the local maximum. The comparison of Fig. 5 with Fig. 4 reveals that the maximum bandwidth curve (Fig. 5) lies above the maximum gain curve (Fig. 4) as expected from Fig. 2. The optimized values of the dielectric constant and the wall radius are thus given by (from Fig. 5) ϵ=12.6 and R_c/R_c^0 = 0.77. These parameters are to be compared to ϵ=15.2 and R_c/R_c^0 = 0.63 for the wall clad configuration.

The dependence of the gain (and the bandwidth) on the beam center location (R_0) is illustrated in Fig. 6. Here the maximum gain is plotted against the beam location R_0. The physical lower limit of the beam location is depicted by a dotted vertical line in the figure. The maximum gain monotonically decreases as the beam location R_0 is increased. This dependency of the gain is expected, since the instability driving electric field tends to concentrate inside the dielectric center rod. Thus, as the beam is located as close as possible to the edge of the center rod, the gain is increased. At the same time, the SWM is also enhanced by locating the beam as close as to the dielectric material [2], [4], [6]. This similar behavior of the gain for the SWM and IWM with respect to the beam location is contrast to those for the wall clad case. There, since the dielectric is attached to the outer conductor, the IWM gain is increased as R_0 increases. On the other hand, the SWM gain is increased as R_0 reduces [2], [4], [6]. This cooperative nature of the IWM and SWM in the center rod geometry results in the extended IWM region in the frequency space as shown later. The optimized beam location is then given by $R_o \simeq R_d + r_L$. The results of Figs. 4-5 are obtained at this optimized beam location.

The process of the bandwidth optimization is further illustrated in Fig. 7. Here the gain is plotted versus the frequency for Δ=1% and several values of the dielectric constant. The other parameter are optimized as shown. As a reference, the case for ε=1, that is without the dielectric, is also shown (broken curve). The maximum gain is achieved at the single peak for ε=12.2, corresponding to a point in the maximum gain curve in Fig. 2 (case B). For lower ε (ε=11.8) the gain yields a single peak at a lower gain, corresponding to case A in Fig. 2. For higher ε (ε=12.6, 12.8), the beam mode intersects the waveguide mode at two frequencies (case C in Fig. 2), resulting in double

maxima at those frequencies. As ε increases from its maximum gain value (ε=12.2), the gains at the peaks as well as the gain at the valley decrease. Therefore, as ε increases from ε=12.2, the bandwidth, now utilizing both peaks, increases until its maximum is reached at ε=12.6. After the maximum bandwidth, the gain at the valley is too low for the bandwidth to include both peaks (e.g. ε=12.8). This explains why the bandwidth in Fig. 5 decreases abruptly after the maximum value. Fig. 7 also provides information on the contribution of the SWM. Since the gain for ε=1 (without the dielectric, broken line) represents the contribution of the SWM only, we can say that any significant difference from this curve is due to the IWM. We note from Fig. 7 that the significant SWM contribution is for the frequency $\omega/\omega_c \gtrsim 2.0$. This is to be compared with $\omega/\omega_c \gtrsim 1.8$ for the pure IWM and $\omega/\omega_c \gtrsim 1.6$ for the mixed mode operation in the wall clad configuration (see Figs. 3 and 4(a) in Ref. 6). (With the wall clad configuration, the pure IWM operation is achieved with the beam location close to the wall-clad dielectric, and the mixed mode operation with the beam close to the axis, see Ref. 6.) That is, the SWM begins to contribute significantly to the bandwidth at considerably higher frequency with the center rod configuration than with the wall clad configuration, thereby enhancing the frequency range of the IWM for the center rod configuration. In view of the difficulties associated with the SWM, therefore, the center rod configuration is superior to the wall clad geometry.

The foregoing optimization process with respect to the bandwidth for 1% of the axial velocity spread and the beam parameters given in Eq. (9) can be summarized as following:

$$R_d/R_c = 0.20,\ \varepsilon = 12.6,\ R_c/R_c^0 = 0.77$$

$$R_0 = R_d + r_L = 0.35\ R_c. \qquad (11)$$

The optimized bandwidth at Δ=1% is 68% (Fig. 7), of which 51% is due to the IWM, and 17% to the SWM. This proportion is obtained from Fig. 7, attributing the portion for $\omega/\omega_c \geq 2.0$ to the SWM. This bandwidth can be compared to 46% (all IWM) for the pure IWM and 90% (12% IWM + 78% SWM) for the mixed mode with the wall clad configuration [6]. Moreover, the mean frequency $\bar{\omega}$ for the center rod gyroton is $\bar{\omega}/\omega_c = 1.72$, higher than 1.53 for the pure IWM and less than 2.04 for the mixed mode with the wall clad geometry [6]. If we assume that the entire SWM contribution is non-usable, then the bandwidth of the center rod gyrotron is slightly wider than that of the pure IWM and much wider than that of the mixed mode of the wall clad gyrotron.

PERTURBED FIELDS

In previous section we have seen that the frequency range of the IWM for the center rod configuration is wider than that for the wall clad geometry. Since the IWM results from the beam-waveguide mode coupling, its perturbed field profile is very similar to that of the beam-free waveguide, that is, of Bessel function type. On the other hand, the field profile due to the SWM is highly localized near the beam location [2], [4], [6]. Therefore, we can determine the nature of the instability by plotting the field profiles. The instability driving fields $E_{\theta 1}$ and B_{r1} are given in Eqs. (3) and (4). Since the instability occurs near the beam mode, the field profiles are computed at $k=k_B \equiv (\omega-\omega_c/\gamma)/c\beta_z$ for given ω. The quantity k_B is the wavenumber corresponding to $\omega=\omega_B$ (Eq. (8)). In the IWM frequency range, it is shown that $(\omega^2/c^2 - k_B^2) < 0$, hence the Bessel functions J and N with arguments x's (Eq. (7)) now become the modified Bessel functions I and K.

In Fig. 8, the field profiles of $E_{\theta 1}$ and B_{r1} at a particular frequency $\omega=1.7\ \omega_c$ for several values of the dielectric constant are shown. That is, the profiles are drawn from Fig. 7 at that frequency. The fields are normalized such that $\int_0^{R_c} (\varepsilon_j \underline{E}_1^2 + \underline{B}_1^2)\ r dr = R_c^2$. Here $\varepsilon_j = \varepsilon(1)$ for $r < R_d$ ($r > R_d$). The chosen frequency $\omega=1.7\ \omega_c$ corresponds approximately to the transition point between the IWM and SWM (see Fig. 7). We observe in Fig. 8 that the profile for $\varepsilon=1$ (without the dielectric) is highly localized at the beam location (R_0) with a negligible field amplitude in the space ($r < R_d$) where the dielectric rod is supposed to be. This is, of course, expected since the instability for $\varepsilon=1$ is solely due to the SWM. Without the dielectric ($\varepsilon=1$), the waveguide mode is a fast wave ($\omega_G > ck$), and the slow wave IWM is absent. As ε increases the SWM contribution is decreased, as indicated by the decreasing peaks of the field profile at the beam location. The reduced SWM contribution with the

increased ε, in turn, indicates the more enhanced IWM contribution (see Fig. 2). For example, at ε=12.8, the field profile is almost identical to that of the waveguide, indicating nearly pure IWM contribution to the instability. At ω/ω_c = 1.7, the significant SWM contribution is for $\varepsilon \lesssim 11.8$, as can be confirmed from Fig. 7. In terms of difficulties associated with the microwave excitation and collection, the localization of the field strength due to the SWM at the beam location can be a nuisance. However, these difficulties can be eliminated by optimizing the parameter ε, i.e. ε=12.6 in Fig. 8.

The frequency dependenc of the field profile is shown in Fig. 9 for the optimized parameters given in Eq. (11). As the frequency increases, the peak at the beam location (R_0) is more pronounced. This indicates that the contribution of the SWM is nearly negligible for $\omega/\omega_c \lesssim 1.8$ and is significant for $\omega/\omega_c \gtrsim 2.0$, confirming the similar conclusion from Fig. 7. This profile can be compared with that for the mixed mode with the wall clad geometry (Fig. 6 in Ref. 6), where the SWM is significant for $\omega/\omega_c \gtrsim 1.6$. We thus again find that the center rod configuration extends the IWM region further than the wall clad gyrotron.

CONCLUSION

We have investigated the wide band capability of the gyrotron with a dielectric material used as a center rod. After deriving the dispersion relation for the azimuthally symmetric, TE perturbations, we have found the optimization conditions on the physical parameters for a wide bandwidth at a small axial velocity spread (Δ=1%).

The results of the optimization processes and the comparison with the wall clad configuration can be summarized in Table 1. All values are obtained with the beam parameters in Eq. (9). The center rod configuration allows larger wall dimension, lower dielectric constant, and thicker center rod compared to the wall clad configuration. The gain for the center rod configuration is slightly lower than that of the pure IWM for the wall clad configuration, but higher than that of the mixed mode for the wall clad configuration. The bandwidth is wider than the pure IWM, but narrower than the mixed mode. However, in terms of difficulties associated with the SWM, the center rod configuration proves to be superior in the bandwidth to both the pure IWM and the mixed mode. This advantage comes from the extended IWM frequency range in the center rod configuration.

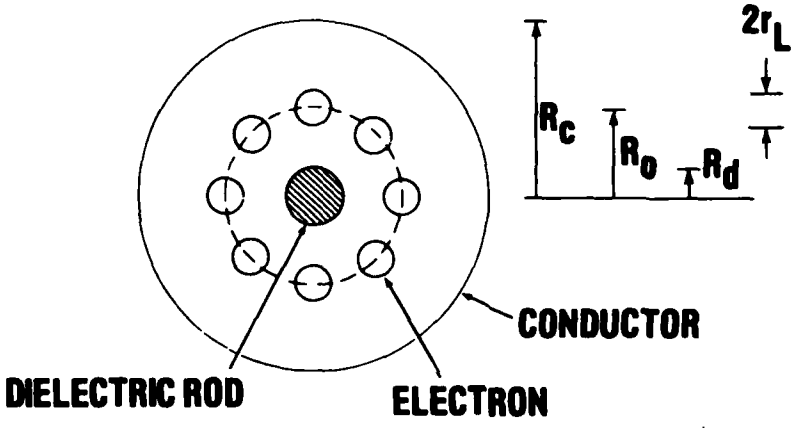

Figure 1 Cross section of a gyrotron with a dielectric center rod

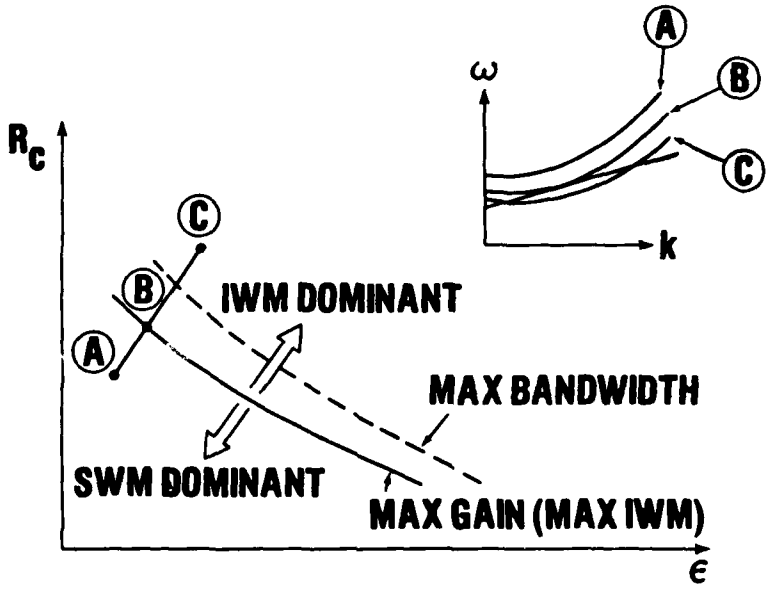

NOTE: The dispersion curves for the parameters represented by A, B and C are shown in the upper corner. The maximum bandwidth curve (broken) is located above the maximum gain curve in R_c-ϵ space.

Figure 2 Schematic diagram of the mode characteristics in the space of the conducting wall radius (R_c) and the dielectric constant (ϵ)

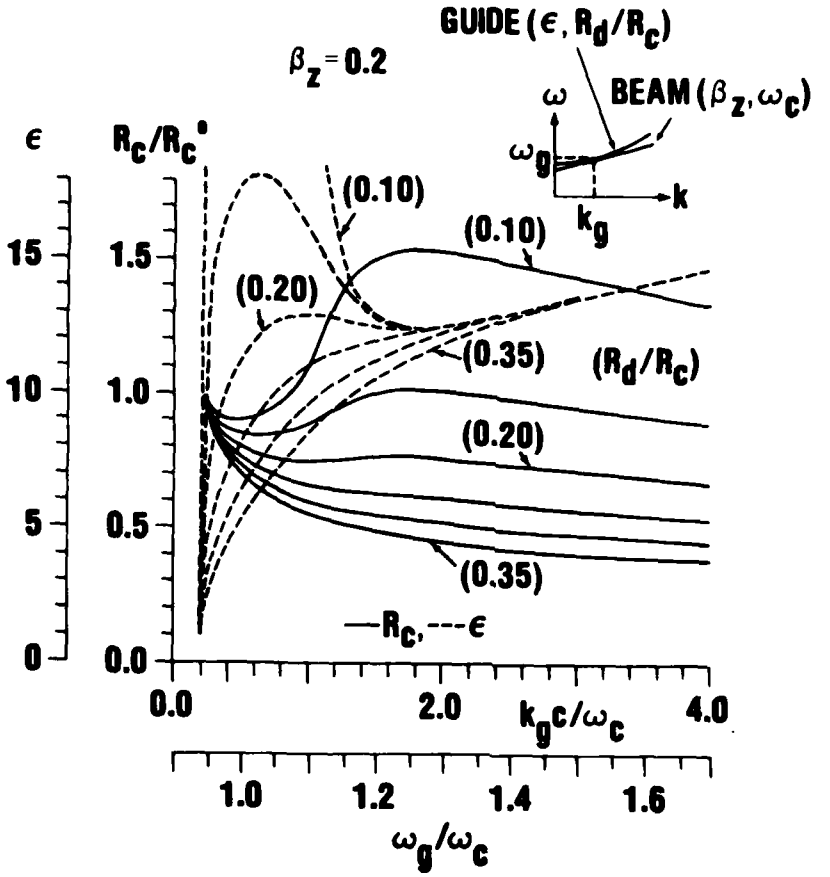

NOTE: The values of R_c and ϵ that make the beam mode graze the waveguide mode (upper corner) are shown for several values of the thickness parameter (R_d/R_c).

Figure 3 **Grazing conditions on the conducting wall radius (R_c, —) and the dielectric constant (ϵ, ---)**

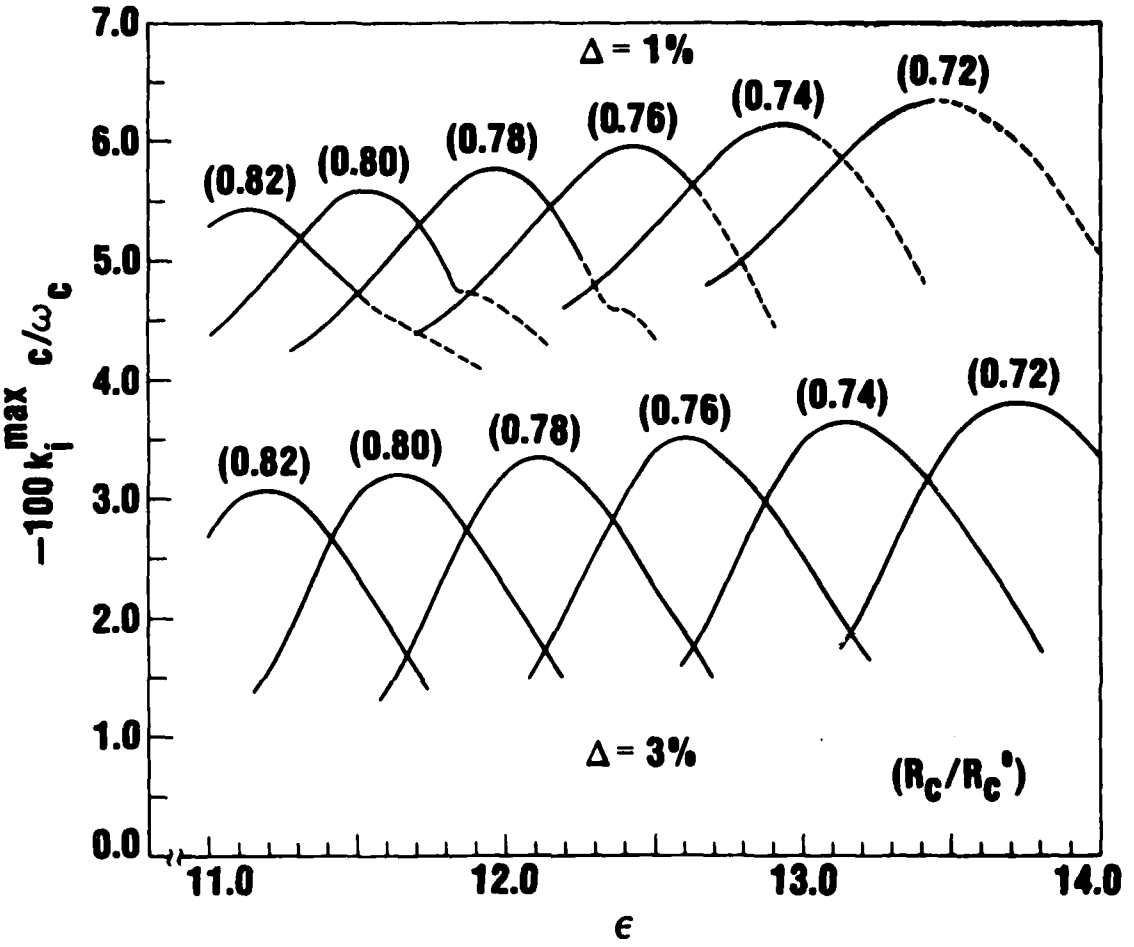

NOTE: For Δ=1%, the gain exhibits double maxima at high ε denoted by broken lines.

Figure 4 Plots of the maximum gain ($-k_i^{max}$) vs. the dielectric constant (ε) for several values of the conducting wall radius (R_c), and at two different axial velocity spreads (Δ)

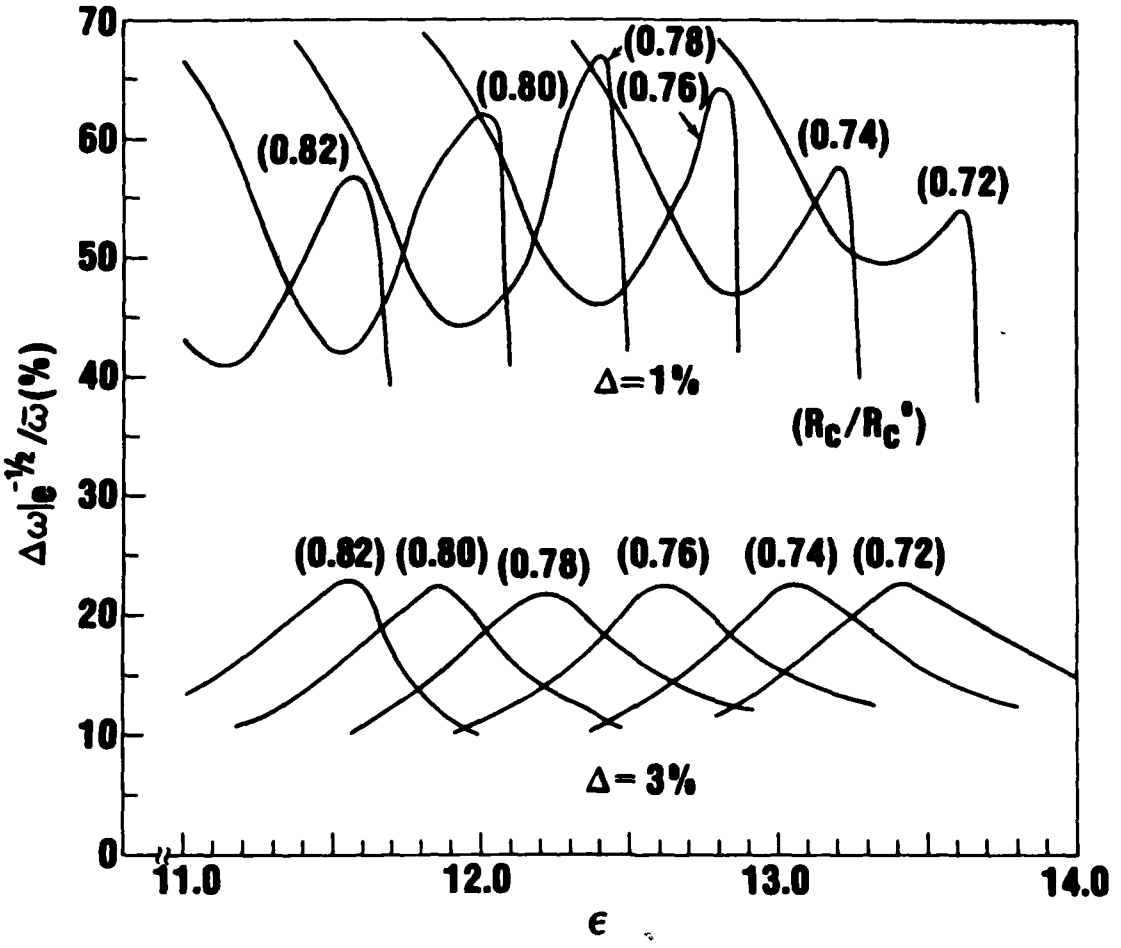

Figure 5 Plots of the bandwidth (Δω) vs. the dielectric constant (ε) for several values of the conducting wall location (R_c), and two different velocity spreads (Δ)

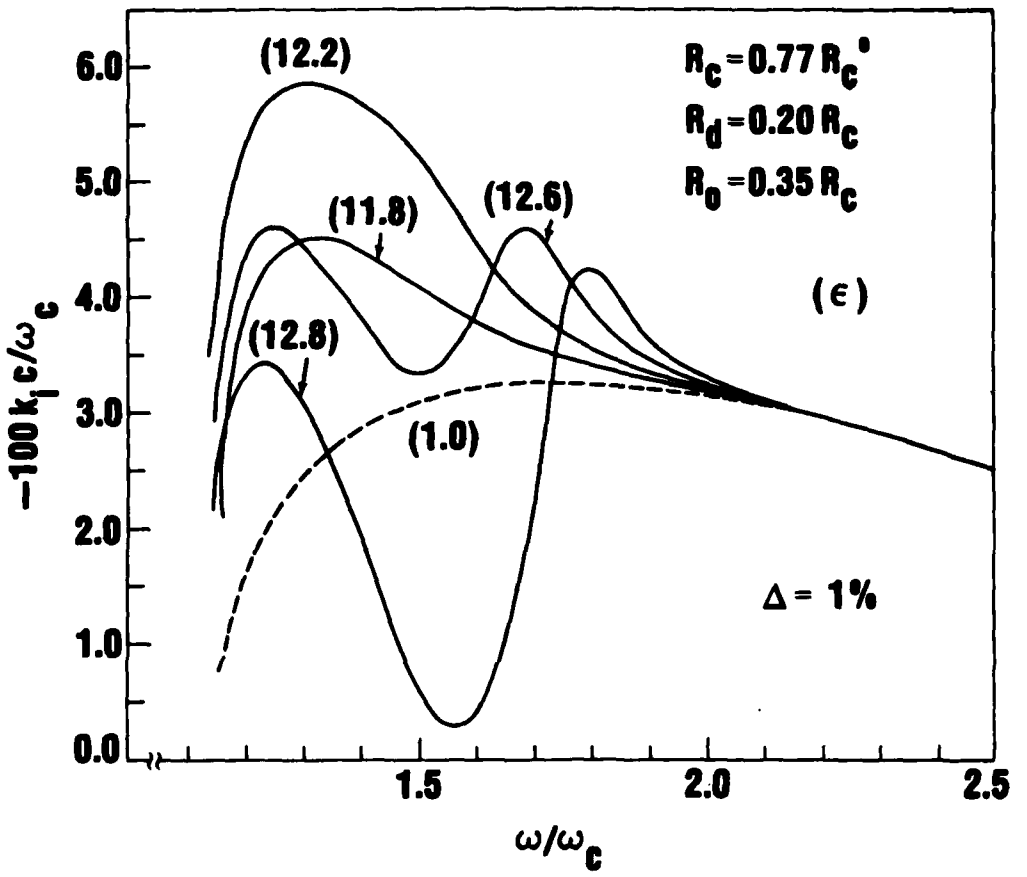

NOTE: The broken vertical line corresponds to the physical lower limit of R_0, where the inner edge of the beam touches the dielectric rod.

Figure 6 Dependence of the maximum gain ($-k_i^{max}$) on the beam center location (R_0)

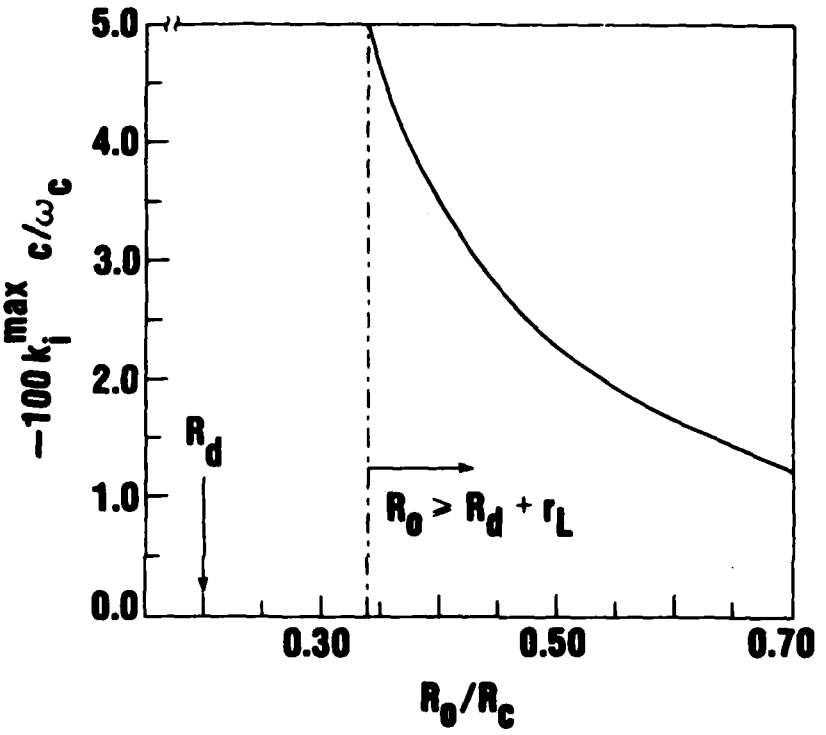

Figure 7 Plots of the gain ($-k_i$) vs. the frequency (ω) for several values of the dielectric constant (ε). Other optimized parameters are as shown. The broken line ($\varepsilon = 1.0$) corresponds to the absence of the dielectric rod

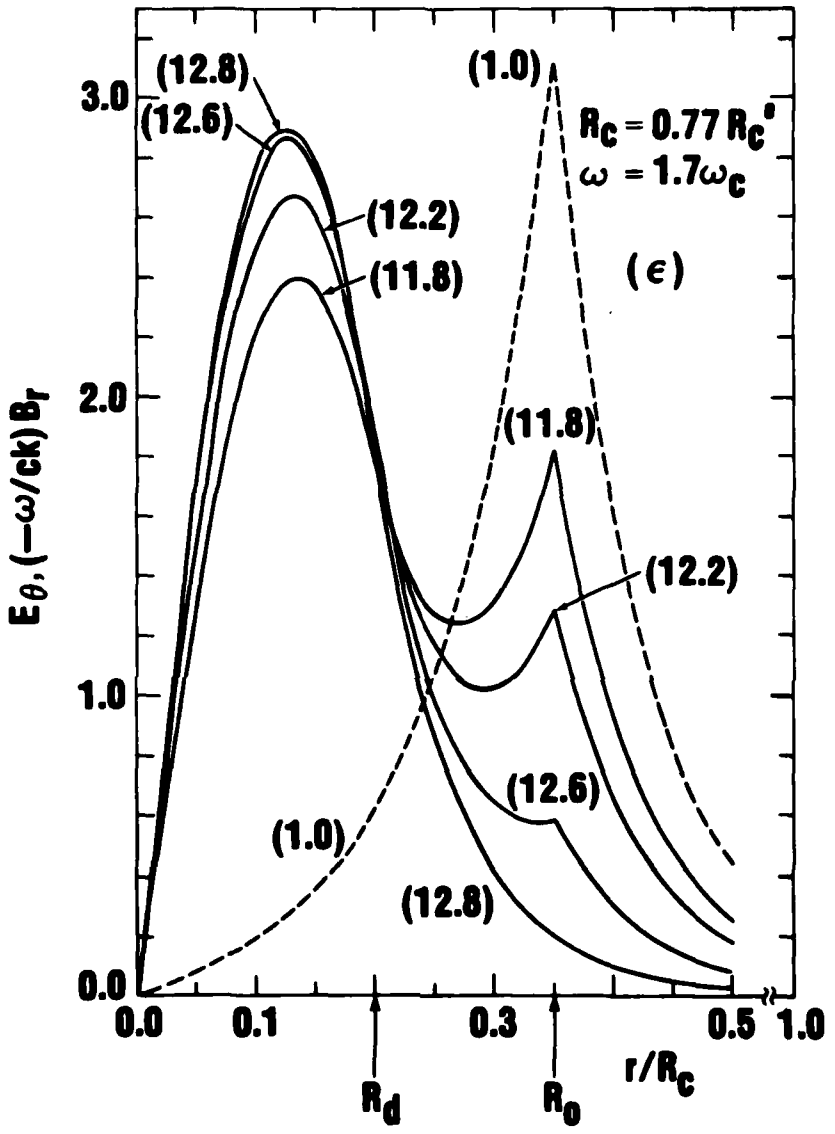

Figure 8 Perturbed field profiles for several values of the dielectric constant (ε) for ω/ω_c = 1.7 and parameters otherwise identical to those in Fig. 7

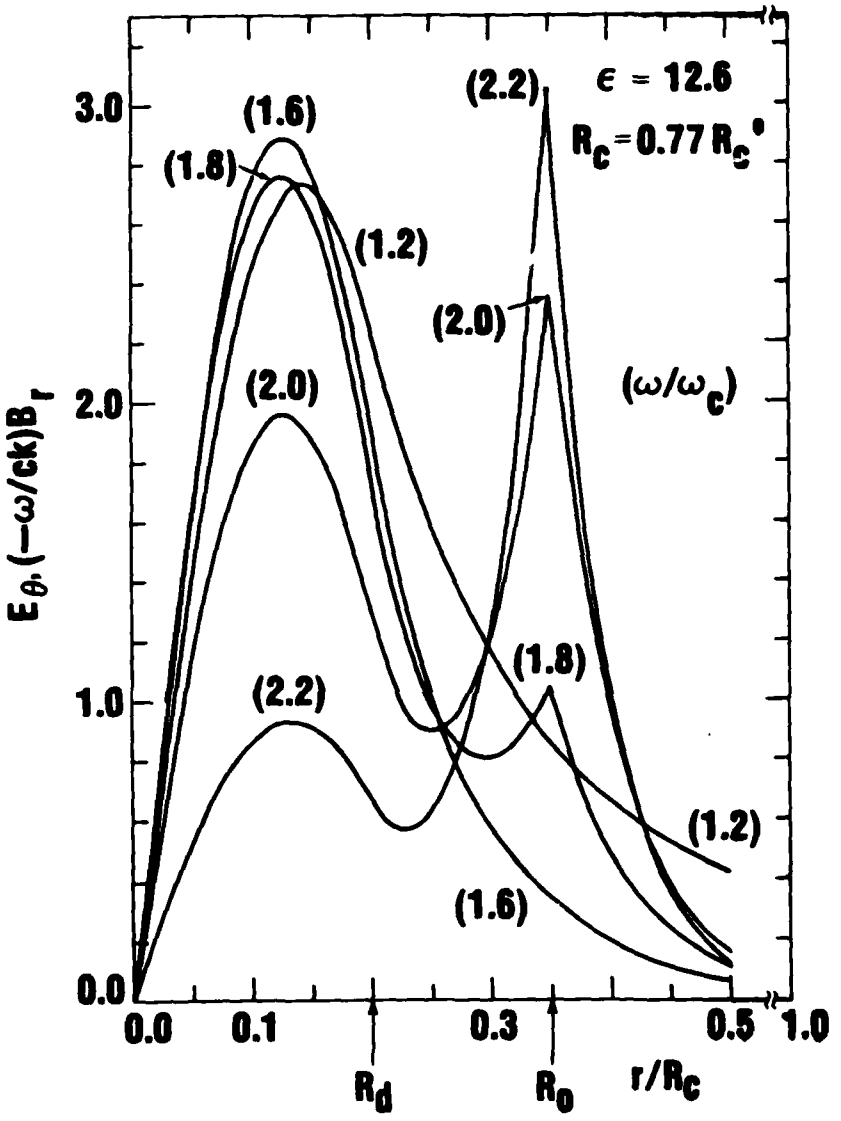

Figure 9 Perturbed field profiles for several values of the frequency (ω) at the optimized parameters given in Eq. (11)

Table 1 Comparison of the bandwidth-optimized dielectric gyrotron

Dielectric Used As	Center Rod	Wall Clad	
		Pure IWM	Mixed Mode
ϵ	12.6	15.2	
R_c/R_c^0	0.77	0.63	
Thickness Ratio	$R_d/R_c = 0.20$	$R_w/R_c = 0.85$	
Beam Location	$R_0 \gtrsim R_d + r_L$	$R_0 \lesssim R_c - r_L$	$R_0/R_c = 0.38$
$-100\ k_i^{max}\ c/\omega_c$	4.6	5.6	3.8
Significant SWM Contribution	$\omega/\omega_c \gtrsim 2.0$	$\omega/\omega_c \gtrsim 1.8$	$\omega/\omega_c \gtrsim 1.6$
Mean Frequency	$\bar{\omega}/\omega_c = 1.72$	$\bar{\omega}/\omega_c = 1.53$	$\bar{\omega}/\omega_c = 2.04$
Bandwidth (IWM + SWM)	68% (51 + 17)	46% (46 + 0)	90% (12 + 78)
$-100\ k_i^{max}\ c/\bar{\omega}$	2.7	3.9	1.8

ACKNOWLEDGMENT

This research was supported in part by an Independent Research Fund at the Naval Surface Weapons Center, and in part by the Office of Naval Research.

REFERENCES

[1] H. S. Uhm and R. C. Davidson, Phys. Fluids, vol. 23, p. 2538, 1980.

[2] J. Y. Choe, H. S. Uhm, and S. Ahn, J. Appl. Phys. (in press, Ms. #R-1251, 1981); see also NRL Memo. Rep. 4460, 1981.

[3] H. Keren, J. L. Hirschfield, S. Y. Park, K. R. Chu, and J. M. Baird, Proc. Fifth Int. Conf. Infrared Millimeter Waves, p. 96, 1980.

[4] J. Y. Choe, H. S. Uhm, and S. Ahn, IEEE Trans. Nucl. Sci., vol. NS-28, p. 2918, 1981.

[5] A. K. Ganguly and K. R. Chu, NRL Memo. Rep. 4215, 1980.

[6] J. Y. Choe, H. S. Uhm, and S. Ahn, J. Appl. Phys. (in press, Ms. #R-1545, 1981); see also NRL Memo. Rep. 4510, 1981.

[7] H. S. Uhm, J. Y. Choe, and S. Ahn, Int. J. Electronics (to be published, Nov. 1981).

[8] J. Y. Choe, H. S. Uhm, and S. Ahn, "Simple description of amplification mechanism in microwave tubes,"(manuscript in preparation).

DISTRIBUTION

	Copies
Commander Naval Research Laboratory Attn: Dr. Saeyoung Ahn	1
Dr. Wahab A. Ali	1
Dr. J. M. Baird	1
Dr. L. Barnett	1
Dr. O. Book	1
Dr. Jay Boris	1
Dr. K. R. Chu	1
Dr. Timothy Coffey	1
Dr. G. Cooperstein	1
Dr. A. Drobot	1
Dr. Richard Fernslor	1
Dr. H. Freund	1
Dr. M. Friedman	1
Dr. J. Golden	1
Dr. S. Goldstein	1
Dr. V. Granatstein	1
Dr. Robert Greig	1
Dr. Irving Haber	1
Dr. Richard Hubbard	1
Dr. Bertram Hui	1
Dr. Glenn Joyce	1
Dr. Selig Kainer	1
Dr. C. A. Kapetanakos	1
Dr. M. Lampe	1
Dr. Y. Y. Lau	1
Dr. W. M. Manheimer	1
Dr. Don Murphy	1
Dr. Peter Palmadesso	1
Dr. Robert Pechacek	1
Dr. Michael Picone	1
Dr. Michael Raleigh	1
Dr. M. E. Read	1
Dr. C. W. Roberson	1
Dr. J. D. Sethian	1
Dr. William Sharp	1
Dr. J. S. Silverstein	1
Dr. Philip Sprangle	1
Dr. Doug Strickland	1
Dr. C. M. Tang	1
Dr. N. Vanderplaats	1
Washington, DC 20375	

	Copies
Office of Naval Research Attn: Dr. Robert Behringer	1
1030 E. Green Pasadena, CA 91106	
Office of Naval Research Attn: Dr. T. Berlincourt	1
Dr. W. J. Condell	1
Department of the Navy Arlington, VA 22217	
Commander Naval Air Systems Command Attn: Dr. Wasneski	1
Department of the Navy Washington, DC 20361	
Commander Naval Sea Systems Command Attn: Dr. C. F. Sharn	1
Department of the Navy Washington, DC 20362	
Harry Diamond Laboratory Attn: Dr. H. E. Brandt	1
Dr. S. Graybill	1
2800 Powder Mill Road Adelphi, MD 20783	
U. S. Army Ballistic Research Laboratory Attn: Dr. D. Eccleshall	1
Aberdeen Proving Ground MD 21005	
Air Force Weapons Laboratory Attn: Dr. Ray Lemke	1
Kirtland Air Force Base Albuquerque, NM 87117	
Air Force Weapons Laboratory Attn: Dr. D. Straw	1
Kirtland AFB, NM 87117	

DISTRIBUTION (Cont.)

	Copies
U.S. Department of Energy	
Attn: Dr. T. Godlove	1
Dr. M. Month	1
Dr. J. A. Snow	1
Washington, DC 20545	
National Bureau of Standards	
Attn: Dr. Sam Penner	1
Bldg. 245	
Washington, DC 20234	
National Bureau of Standards	
Attn: Dr. Mark Wilson	1
Gaithersburg, MD 20760	
Defense Advanced Research Projects Agency	
Attn: Dr. J. Bayless	1
Dr. Robert Fossum	1
Dr. J. A. Mangano	1
LCOL W. Whitaker	1
1400 Wilson Blvd.	
Arlington, VA 22209	
Science Applications Inc.	
Attn: Dr. Richard E. Aamodt	1
934 Pearl St. Suite A	
Boulder, CO 80302	
Science Applications Inc.	
Attn: Dr. L. Feinstein	1
Dr. Robert Johnston	1
Dr. Douglas Keeley	1
Dr. John Siambis	1
5 Palo Alto Square	
Palo Alto, CA 94304	
Science Applications, Inc.	
Attn: Dr. A. W. Trivelpiece	1
San Diego, CA 92123	
Science Applications, Inc.	
Attn: Dr. Ron Parkinson	1
1200 Prospect Street	
P.O. Box 2351	
La Jolla, CA 92038	

	Copies
TRW	
Defense and Space Systems Group	
Attn: Dr. D. Arnush	1
Dr. M. Caponi	1
1 Space Park	
Redondo Beach, CA 90278	
Lawrence Livermore National Laboratory	
Attn: Dr. W. A. Barletta	1
Dr. R. Briggs	1
Dr. H. L. Buchanan	1
Dr. Frank Chambers	1
Dr. T. Fessenden	1
Dr. Edward P. Lee	1
Dr. James Mark	1
Dr. Jon A. Masamitsu	1
Dr. V. Kelvin Neil	1
Dr. R. Post	1
Dr. D. S. Prono	1
Dr. M. E. Rensink	1
Dr. Simon S. Yu	1
University of California	
Livermore, CA 94550	
Physics International Co.	
Attn: Dr. Jim Benford	1
Dr. S. Putnam	1
2700 Merced Street	
San Leandro, CA 94577	
Sandia Laboratories	
Attn: Dr. K. D. Bergeron	1
Dr. B. Epstein	1
Dr. S. Humphries	1
Dr. Tom Lockner	1
Dr. Bruce R. Miller	1
Dr. C. L. Olson	1
Dr. Gerold Yonas	1
Albuquerque, NM 87115	
La Jolla Institute	
Attn: Dr. K. Brueckner	1
Prof. N. M. Kroll	1
P.O. Box 1434	
La Jolla, CA 92038	

DISTRIBUTION (Cont.)

	Copies
Mission Research Corp.	
Attn: Dr. Neal Carron	1
Dr. Conrad Longmire	1
735 State Street	
Santa Barbara, CA 93102	
Mission Research Corp.	
Attn: Dr. B. Godfrey	1
1400 San Mateo Blvd, S.E.	
Suite A	
Albuquerque, NM 87108	
McDonnell Douglas Corp.	
Attn: Dr. M. Greenspan	1
Dr. J. Carl Leader	1
P. O. Box 516	
St. Louis, MO 63166	
Los Alamos National Lab.	
Attn: Dr. Barry Newberger	1
Dr. L. E. Thode	1
Mail Stop 608	
Los Alamos, NM 87544	
Los Alamos Scientific Lab.	
Attn: Dr. H. Dreicer	1
Dr. R. J. Faehl	1
Los Alamos, NM 87544	
Pulse Sciences, Inc.	
Attn: Dr. Sid Putnam	1
1615 Broadway, Suite 610	
Oakland, CA 94612	
National Science Foundation	
Attn: Dr. R. Hill	
Physics Division, #341	
Washington, DC 20550	
W. J. Schafer Associates, Inc.	
Attn: Dr. Edward Cornet	1
1901 North Fort Myer Dr.	
Arlington, VA 22209	

	Copies
Austin Research Associates	
Attn: Prof. W. E. Drummond	1
Dr. M. Lee Sloan	1
Dr. James R. Thompson	1
1901 Rutland Drive	
Austin, TX 78758	
Western Research Corporation	
Attn: Dr. Franklin Felber	1
8616 Commerce Avenue	
San Diego, CA 92121	
Jaycor	
Attn: Dr. J. U. Guillory	1
Dr. D. Tidman	1
205 S. Whiting Street	
Alexandria, VA 22304	
Varian Associates	
Attn: Dr. Howard Jory	1
611 Hansen Way	
Palo Alto, CA 94303	
Lawrence Berkeley Lab.	
Attn: Dr. Denis Keefe	1
Dr. Hogil Kim	1
Dr. Hong Chul Kim	1
Dr. Kwang Je Kim	1
Dr. L. J. Laslett	1
Dr. G. R. Lambertson	1
Dr. A. M. Sessler	1
Dr. L. Smith	1
1 Cyclotron Road	
Berkeley, CA 94720	
Stanford Linear Accelerator Center	
Attn: Dr. Philip Morton	1
P.O. Box 4349	
Stanford, CA 94305	
AVCO - Everett Research Laboratory, Inc.	
Attn: Dr. Richard Patrick	1
2385 Revere Beach Pkwy	
Everett, MA 02149	

DISTRIBUTION (Cont.)

	Copies
Oak Ridge National Lab	
Attn: Dr. J. A. Rome	1
Oak Ridge, TN 37850	
University of California at Los Angeles	
Attn: Prof. F. Chen	1
Dr. A. T. Lin	1
Dr. J. Dawson	1
Dr. C. S. Liu	1
Dr. Edward Ott	1
Los Angeles, CA 90024	
University of Maryland	
Attn: Dr. W. Destlar	1
Dr. C. S. Liu	1
Dr. Won Namkung	1
Dr. E. Ott	1
Prof. M. Reiser	1
Dr. Moon-Jhong Rhee	1
Dr. C. D. Striffler	1
College Park, MD 20742	
Columbia University	
Attn: Prof. P. Diament	1
Prof. S. Schlesinger	1
New York, NY 10027	
North Carolina State University	
Attn: Prof. W. Doggett	1
Dr. Jin Joong Kim	1
P. O. Box 5342	
Raleigh, NC 27650	
Massachusetts Institute of Technology	
Attn: Prof. George Bekefi	1
Dr. K. J. Button	1
Prof. R. Davidson	1
Dr. R. Temkin	1
77 Massachusetts Avenue	
Cambridge, MA 02139	

	Copies
University of California	
Attn: Dr. Gregory Benford	1
Dr. A. Fisher	1
Prof. N. Rostoker	1
Physics Department	
Irvine, CA 92717	
Yale University	
Attn: Dr. I. B. Bernstein	1
Dr. J. L. Hirshfield	1
Mason Laboratory	
400 Temple Street	
New Haven, CT 06520	
Cornell University	
Attn: Prof. H. Fleischmann	1
Prof. D. Hammer	1
Prof. R. V. Lovelace	1
Prof. J. Nation	1
Prof. R. Sudan	1
Ithaca, NY 14850	
University of Texas at Austin	
Attn: Dr. M. N. Rosenbluth	1
Institute for Fusion Studies	
RLM 11.218	
Austin, TX 78712	
Stevens Institute of Technology	
Attn: Prof. George Schmidt	1
Physics Department	
Hoboken, NJ 07030	
Dartmouth College	
Attn: Dr. John E. Walsh	1
Department of Physics	
Hanover, NH 03755	
Defense Technical Information Center	
Cameron Station	
Alexandria, VA 22314	12

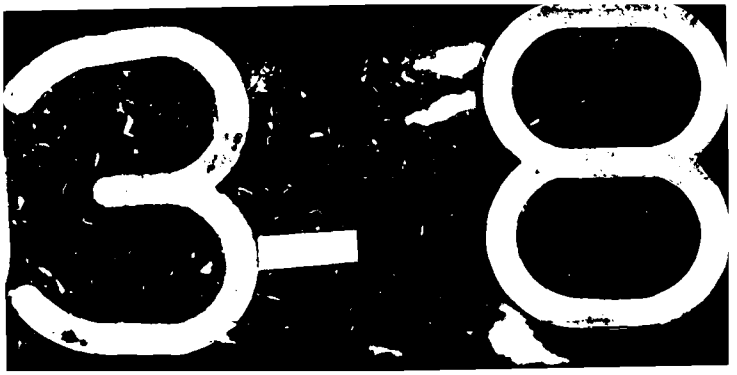
3-8